Numeric Multi-Dimensional (r, z, t) Analysis Method for Compact Yb^{3+}:YAG End-Pumped, Passively Q-Switched Lasers

Stephen R. Chinn, *Life Senior Member, IEEE*, Jeffrey H. Leach[ID], Chris McIntosh, A. D. Hays, and Lew Goldberg

Abstract—We have applied a new simplified combination of numerical methods for studying the time and three-dimensional space dependence of quasi-three-level Yb^{3+}:Yttrium Aluminum Garnet (YAG) end-pumped lasers passively Q-switched by a Cr^{4+}:YAG saturable absorber. We base our 3-D model on iterative, efficient, time- and space-dependent numerical propagation of the optical field through the laser cavity. The complex-valued laser field is coupled to the Yb^{3+}:YAG and Cr^{4+}:YAG media via complex optical permittivities, which are subsequently altered by gain/loss intensity saturation. The calculation is simplified using the radial symmetry of the system, with the cavity round-trip time as the smallest increment for updating the permittivities. We also include the effects of field diffraction in an intracavity air gap. For specified CW spatial pump conditions, self-consistent repetitively pulsed solutions for the laser field in a flat-flat or flat-convex mirror cavity are found with no *ad hoc* laser mode size or shape assumptions; these solutions are not Gaussian modes. We concentrate on compact lasers with multi-Watt average output power, operating at modest pulse energy (∼1.0 mJ), high repetition rate (∼5 kHz) and short pulse duration (∼1.5 ns). Typical room-temperature pump-to-laser slope power efficiencies exceeding 50% are predicted, depending on laser pump and cavity loss parameters. Model results agree well with recently published experimental data.

Index Terms—Solid lasers, ytterbium, optical pulses, Q-switching, laser resonators, finite difference methods.

I. INTRODUCTION

ACTIVELY Q-switched Yb^{3+}:YAG lasers [1] have evolved into so-called micro-lasers or microchip lasers of Yb^{3+}:YAG (or their ceramic variants) passively Q-switched by Cr^{4+}:YAG saturable absorbers [2]–[4]. Typically, these end-pumped systems use light from high- power diode lasers coupled through large-core multi-mode fibers and refocused into the Yb^{3+}:YAG, coaxial with the lasing direction. Different applications have unique requirements, so a wide range of

laser sizes and parameters are of interest. Device modeling and simulation play a useful role in understanding laser behavior and optimizing parameters to obtain the best performance. Often, the diode pump lasers are CW, and result in repetitive passively Q-switched output pulses, as described in this work. The Yb^{3+} lasing ions have a quasi-three-level system for transitions between the two upper and lower Yb^{3+} electronic state manifolds, with substantively different behavior from the commonly-used Nd^{3+} low-absorption four-level laser system. Although we discuss the specific Yb^{3+} laser system, the methods are well suited to other quasi-3-level rare-earth ions such as Tm^{3+} or Ho^{3+}, with significant ground state absorption. Similarly, other passive Q-switch materials can be treated, as long as an easily saturated ground-state absorption matches the laser emission, and the population rate equations are relatively simple, with excited-state decay time meeting the requirements for fast, repetitive pulsing.

In most of our cited references, a common practice for analyzing the passively Q-switched Yb^{3+} devices is to assume that the pump and laser mode have uniform transverse (i.e. top-hat plane-wave) distributions with a known spot size, or a uniform or Gaussian pump producing a Yb^{3+}:YAG Gaussian laser mode with known waist. In papers on similar Nd lasers which assume non-uniform pump profiles, it is common to use the transverse overlap between the pump and an assumed Gaussian laser mode. The temporal behavior is found by solving the coupled differential rate equations for the laser population inversion and Cr^{4+} electronic level population densities (using uniform or longitudinally averaged values) and photon densities. Standard ordinary differential equation computer codes can quickly produce high-temporal-resolution solutions, even in such a stiff system of equations. Other simpler analyses [5], [6] (albeit for Nd:YAG) perform analytic integration of the time-dependent laser variables (assuming transverse uniformity and longitudinal gain averaging) to find non-linear or transcendental equations relating pre- and post-Q-switch gains. Analysis by Okhrimchuk and Shestakov [7] is based on r- and t- dependent variables, but averages over longitudinal z-dependence. A useful approximation for Q-switched 3-level systems by Nabors [8] uses the round-trip-time (t_{RT}) as a scaling interval, with the assumption that the gain exponent has only small changes in t_{RT}. This enabled simplified results from analytic time-integration over the pulse (although without examining a passive Q-switch). We will use the same round-trip approximation, with an efficient numeric treatment of the

transverse pump and laser modes, longitudinal variation of material parameters, passive Q-switch saturation dynamics, and (usually) an optional cavity air-gap.

The simplified types of time-only analysis methods overlook many effects caused by both lateral and longitudinal non-uniformity in the laser fields and electronic populations. Even with radial integration included by Zhang *et al*. [9], a Gaussian laser field was assumed. There is limited justification for arbitrarily choosing a mode size to match a pump size, to assume a mode shape, or to assume that the laser modes are determined solely by cavity mirror-curvature boundary conditions. For example, the commonly-used flat-flat mirror cavity is inherently unstable, in the absence of gain or thermal guiding.

A contradiction to the validity of Gaussian laser modes for our Yb^{3+}:YAG lasers can be found in the much simpler example of 3-level cw lasers having a longitudinally constant cylindrical gain/loss profile. The eigenmodes of this configuration are Gloge's LP-like modes [10] but with "core/cladding" solutions that are J and K boundary-matched Bessel functions with *complex* eigenvalue arguments. The results presented below for non-uniformly pumped, passively Q-switched lasers show a much closer qualitative resemblance to such gain guided Bessel modes than to Gaussian modes (Fan [11] refers to such generic modes in Yb^{3+}:YAG as "aperture guided"; we prefer the historical precedent of "gain guided", originally applied to modes in oxide-stripe semiconductor lasers [12]).

Thermal modeling of end-pumped lasers in a cw regime and with input parameters for the pump and laser mode sizes was done by Innocenzi *et al*. [13] Other more recent works [14]–[18] on thermal lensing include thermal deposition factors, modal effects and the dioptric lens details. Anashkina and Antonov [19] compare strengths of thermal and gain lensing, but with a constant Gaussian pump, and no calculation of laser modes *per se*. None of these references treat Q-switched operation. Recently, a cryogenically-cooled Yb^{3+}:YAG laser was described [20], producing high-energy pulses in quasi-cw-mode operation with thermal lensing. In the present work we incorporate both the effects of gain and thermal mode confinement in a simultaneous unified approach using a finite-difference beam propagation method (FD-BPM). We contrast this method with "dynamic multimode analysis"[21]–[23] in which a commercial modeling package provides tools for multi-transverse-mode Gaussian expansion of the laser field to investigate laser dynamics. These modal expansion analyses did not include our regime of CW-pumping with passively-Q-switched self-pulsing operation.

Fox and Li [24], [25] laid the foundation for iterative computational integral solution of the spatial modes of empty optical resonators. Later, Hadley *et al*. [26] performed a similar three-dimensional laser field analysis for non-Q-switched 4-level Nd:YAG lasers, but using FD-BPM to find temporally converging steady-state resonant mode solutions. In this work, we present a similar, but simplified, version of a numerical, iterative FD-BPM solution and include the Q-switched pulse dynamics, without the previous concerns [26] for finding the resonant frequencies of the modes, which adds computational burden. The low Q of our typical laser cavities (caused by

Yb^{3+} ground-state absorption, saturable Q-switch loss, and low reflectivity output mirror) and the rapid transient behavior of the media saturation reduce the effects of longitudinal standing-wave-resonance effects. With our new approach, we believe the model is particularly well-suited to passively Q-switched quasi-three-level lasers that operate at repetition frequencies faster than the radiative decay rate, and whose intensity profiles are dominated by the saturated media gain and thermal guiding, rather than the laser cavity reflector curvatures.

We summarize our simple procedure, which combines the results of FD-BPM with a round-trip time-step for media alteration: **(1) the laser fields are propagated for one cavity round-trip** (here using radial FD-BPM, rather than diffraction integrals), **(2) the laser's media are perturbed by the resulting local field intensities and heating**, and **(3) the altered media affect the next iteration of round-trip field propagation**. In essence, this is a quasi-static approximation for the active material properties during a round-trip. There is no absolute minimum for the calculated Q-switched pulse duration, but it must be at least an order-of-magnitude longer than the round-trip time to achieve useful accuracy. The pulse duration will depend on the cavity loss parameters and the differential inversions pre- and post-pulse. Imposing cylindrical radial symmetry on the laser system means that we can solve a 3-spatial-dimension problem using only a single radial coordinate in addition to the longitudinal z dimension (azimuthal transverse angular dependence can also be included in a limited fashion). This simplification from two to one transverse coordinates is a major factor in higher computational efficiency and reduced memory requirements. Complex laser fields are propagated, but we impose no round-trip phase constraints on them since we are not seeking solutions for resonant-frequency cavity modes [26]. The sequence of propagation evolution, graphics 3-D (r, z, and t) displays, and data analysis of multiple pulses can typically be executed on a standard computer in a few minutes within a general high-level compiled coding environment [27], chosen primarily for its interactive graphics interface and analytic capabilities. Any similar scientific coding/graphics environment should suffice, particularly if an efficient tri-diagonal matrix solver (discussed in Section II) can be used. The final code offers major advances in accuracy and flexibility over the simpler examples mentioned above, particularly in its capability to incorporate the major effects of spatial non-uniformities. It is less simple and slower to execute, but even some of the quasi-analytic models may require numerical techniques such as solving non-linear equations or ordinary temporal differential equations.

Displaying selected fields as they evolve is a useful aid to understanding the physics of the dynamic laser system. For example, the execution time (using a 4-core (Intel) 3.4GHz desktop computer), with selected graph and progress monitor updates for a 12-Q-switched pulse sequence, at maximum pump power and highest repetition rate (described below) was 670s. This included automatic analysis of relevant laser outputs.

We previously developed a similar FD-BPM method for *single-pulse* analysis [28] of a 3-level (Er,Yb) glass laser
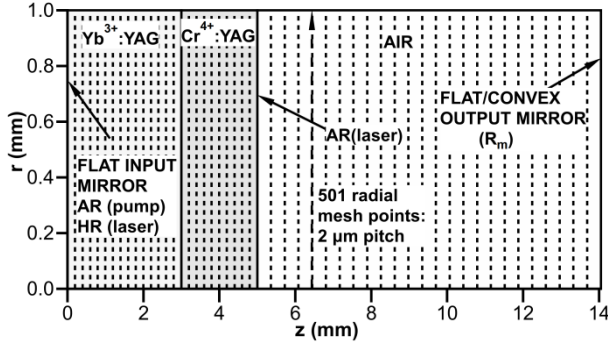
Fig. 1. Schematic typical laser cavity with computation grid. AR = anti-reflection coting, HR = high-reflection coating.

system with Co^{2+} spinel absorber; the details of the present laser configuration and round-trip iteration procedure differ significantly from that case. For our Yb^{3+}:YAG laser, there is a larger mode size, higher pulse energy, and continuous repetitive multi-pulse operation. These characteristics required a greatly revised calculation mesh configuration, and the development of the improved algorithm and time-step iteration strategy.

II. FINITE-DIFFERENCE BEAM PROPAGATION METHOD

A major simplification in our approach is to use the round-trip time increment rather than a z-slice time increment. In addition, we include an air-gap region at the output end of the laser, where a low-reflectance flat or curved output mirror is located. In most cases we have included a curved convex output coupler intended to offset thermal lensing effects, discussed below. Fig. 1 shows a diagram of a typical laser configuration (omitting the fiber-coupled focused pump input), including the calculation mesh description. For clarity, the longitudinal plane separations are shown at twice their scaled values.

To allow for simpler calculations and future iteration methods, all the z mesh increments have equal propagation times. The radial mesh point increments are 2μm. The particular configuration in Fig. 1 has equal total propagation times in the air gap and YAG media, but this is not a model constraint. Small displacement of the saturable absorber away from the Yb^{3+}:YAG crystal within the cavity should have negligible effect. We choose to model the monolithic combination of YAG laser and Q-switch media because of the simplification it affords to the computer propagation code, without significantly altering the results.

FD-BPM provides a solution of the Helmholtz electromagnetic-field propagation equation with slowly varying envelope approximation (SVEA), defined on discrete meshes in the transverse and longitudinal directions. Hadley [29] has shown that improved high-angle accuracy can be obtained using higher-order corrections caused by $\partial^2/\partial z^2$ in the total differential propagator. In particular, the correction with the (1,1) Padé operator achieves higher accuracy than the usual paraxial method, with negligible calculation burden (the difference equations described below remain tri-diagonal). The continuous version of the (1,1) Padé

propagation equation can be written as

$$\frac{\partial E}{\partial z} = \left(\frac{-\frac{i}{2k} P}{1 + \frac{i}{2k} \frac{\partial}{\partial z}} \right) E. \tag{1}$$

If the z-derivative term in the denominator of (1) is removed, the equation has the simpler standard paraxial form. The method neglects polarization effects, and the envelope solutions have scalar values. In this sense our solutions are analogous to the linearly-polarized (LP) weakly guided modes of cylindrical optical wave-guides [10].

In (1), the transverse operator P in the propagation medium (expressed in radial coordinates) is [30]

$$P = \frac{\partial^2}{\partial r^2} + \frac{1}{r} \frac{\partial}{\partial r} - \frac{l^2}{r^2} + k_o^2 \left(n^2 - \bar{n}^2 \right), \tag{2}$$

and E is the electric-field *envelope* after factoring out constant-parameter z-varying exponential phase and gain/loss terms. Non-italic E will be used for the total fields with the baseline gain/loss exponential factors restored. In cylindrical coordinates, the azimuthal phase variation is characterized by integer l (an effective angular momentum). We consider only $l = 0$ and $l = 1$ terms. Other variable definitions are summarized below:

λ_0 = free-space wavelength
$k_0 = \lambda_0/2\pi$ = free-space wave-vector
$n = n(r,z)$ = complex, spatially varying refractive index
$\bar{n}$ = constant real background index of medium

$$k = \bar{n} k_0$$

$n^2 - \bar{n}^2 \simeq \text{complex}\{2\bar{n} n_{re}(r, z), (\bar{n}\lambda_0/2\pi) g\}$
g_{Yb}, g_Q = perturbed media power gain coefficients (uniform background loss subtracted)
Δr = radial mesh increment (index m)
Δz = longitudinal mesh increment (index q)

$$\xi = \frac{1 - ik\Delta z}{1 + ik\Delta z}, \quad |\xi| = 1$$

$$\hat{\rho} = \frac{4k^2 (\Delta r)^2}{1 + ik\Delta z}$$

$$\varsigma_m^q = (\Delta r k_0)^2 \left[(n_m^q)^2 - \bar{n}^2 \right] - (l/m)^2 - 2$$

$$= \text{complex permittivity difference at } r, z.$$

In each uniform-medium region of the laser and Q-switch, the z-dependence of the complex permittivity is caused by the z variation of the absorbed Yb^{3+}:YAG pump and by laser intensity saturation of the Yb^{3+} and Cr^{4+} population inversions. Changes to the real part of the time-average permittivity come from thermal changes to the real part of the effective refractive index n_{re}, driven by the time-average energy deposition from the quantum defect between pump and laser photon energies.

Standard discrete differencing is applied to (1) and (2); collecting terms with common longitudinal indices q (shown as super-script) and radial indices m (sub-script) gives an implicit Crank-Nicholson matrix difference equation (note that we index from $m = 0$; negative index field terms are omitted,

as are those beyond the large-m boundary):

$$(1 - 1/2m)\, E_{m-1}^{q+1} + \left(\hat{\rho} + \zeta_m^{q+1}\right) E_m^{q+1} + (1 + 1/2m)\, E_{m+1}^{q+1}$$
$$= \xi\, (1 - 1/2m)\, E_{m-1}^q + \left(\hat{\rho} + \xi\zeta_m^q\right) E_m^q + \xi\, (1 + 1/2m)\, E_{m+1}^q \tag{3}$$

Equation (3) is an implicit tri-diagonal set of linear equations over radial index m, where the radial solution for E at z-step $q+1$ can be found using an input vector derived from the field at the previous z-step q. This may be represented as the inner product of a LHS tri-diagonal matrix (whose coefficients are in parentheses) with an unknown column vector $\vec{E}^{q+1}$ equated to an input source column vector (right-hand side, with all E-vector components indexed by subscript). The physical direction of a z-step may be positive or negative depending on the propagation direction of the local round-trip field.

Matrix inversion is an inefficient solution method in this case; standard computation libraries have fast and efficient solvers for such sparse tri-diagonal systems. Before applying (2) or (3), their indeterminate form at $r = 0$ (or $m = 0$) must be evaluated using L'Hôpital's rule, as described in [30]. The m-dependent matrix (LHS) and vector (RHS) coefficients in (3) must be modified at $r = 0$ depending on the value of l, in order to remove the apparent singularity. For the radial coordinate, at $r = 0$ these changes constrain the $l = 0$ E solutions to have zero derivative (w.r.t. r) and the $l = 1$ solutions to have zero value.

The permittivity functions in the laser, Q-switch, and air-gap regions vary in their detail but not general form. We use simplified internal units for the fields such that Intensity [in units of W $/\mu m^2$] $= \frac{1}{2}\bar{n}_{re}\,|E|^2$, to conserve intensity across media boundaries.

At the output coupler longitudinal boundary, the laser field is reflected using the amplitude reflection coefficient. If the coupler is curved, an additional radial quadratic phase factor is included in the complex coefficient for the reflected field; a thin-lens quadratic phase term from the plano-convex coupler shape multiplies the outward transmitted field.

The boundary conditions at the outer edge of the radial computation grid are important for suppressing spurious inward-traveling reflected fields caused by the grid truncation. This problem is well known, and we use a method based on Hadley's transparent boundary condition (TBC) [31], [32]. Its simplest form for Cartesian coordinates uses an oblique plane wave approximation for the laser field near the boundary, and adjusts the edge BPM field coefficients at each propagation step to make the solution appear to be freely radiating. Yamauchi *et al.* [30] cite this method, but give no example of its application to the cylindrical BPM problem. For their related finite-difference time-domain method (FD-TDM) procedure, they use an absorbing boundary layer. The TBC formalism has not been rigorously justified in cylindrical coordinates. We use an *ad hoc* variant of Hadley's method with radial cylindrical field weighting, and a linear combination of two sequential-z TBC field-ratios. The TBC and the intrinsic absorption of Yb^{3+} and Cr^{4+} away from the pump and laser
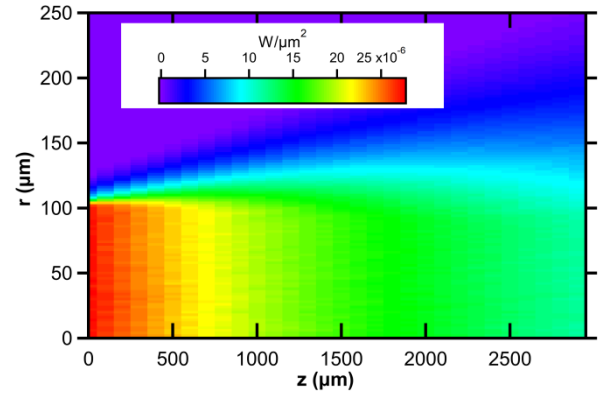

Fig. 2. *Un-attenuated* pump intensity in Yb^{3+}:YAG from ray-trace analysis at 1W input, approximate 2× fiber core magnification.
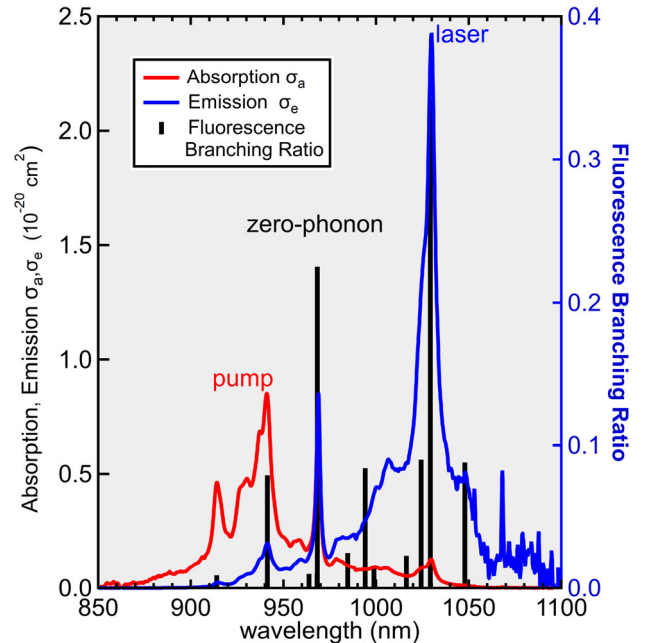

Fig. 3. Yb^{3+}:YAG absorption and emission spectra, from measured absorption data (at $T = 300K$) and the McCumber model. Branching ratios from [46].

mode regions effectively suppress fractional lateral intensity reflections near the radial grid boundary to $<1 \times 10^{-8}$.

III. MEDIA POPULATION RATE-EQUATIONS

In the Yb^{3+}:YAG laser crystal, the Yb^{3+} ions have two vibronically-broadened crystal-field manifolds, the upper $^2F_{5/2}$ and the lower $^2F_{7/2}$, roughly 10500 cm^{-1} apart. We must model simultaneous processes of stimulated emission and absorption at the 940-nm pump wavelength and at the 1030-nm laser wavelength. In describing the laser's material properties and rate equations, we use the notation and values in the table below.

Un-pumped Yb^{3+} has an initial unsaturated power absorption coefficient $\alpha_{0P} = N_{Yb}\sigma_{aP}$ at the pump wavelength and $\alpha_{0L} = N_{Yb}\sigma_{aL}$ at the laser wavelength. The absorption cross-sections in Table I come from data of Brown *et al* [33]. We derive the weighted, spectrally-mirrored emission cross-sections in Table I and Fig. 3 below from the

TABLE I
SYMBOL DESCRIPTIONS AND VALUES

Symbol	Description	Units	Value
σ_{aP}	Pump Yb absorption cross-section	cm^2	7.93×10^{-21}
σ_{eP}	Pump Yb emission cross-section	cm^2	1.74×10^{-21}
σ_{aL}	Laser Yb absorption cross-section	cm^2	1.28×10^{-21}
σ_{eL}	Laser Yb emission cross-section	cm^2	2.42×10^{-20}
τ_{Yb}	Yb spontaneous emission lifetime	s	0.967×10^{-3}
N_{Yb}	Yb ion density (laser); 10% doping	cm^{-3}	1.39×10^{21}
ρ	Fractional Yb upper manifold population		variable
σ_{gQ}	Q-switch Cr ground state absorption cross-section	cm^2	4.6×10^{-18}
σ_{XQ}	Q-switch Cr excited state absorption cross-section	cm^2	8.2×10^{-19}
τ_{Cr}	Cr^{4+} decay time	s	3.4×10^{-6}
μ	Fractional Cr^{4+} inversion		variable

measured absorption data [33] using the standard McCumber model [34]. This model implies internal thermal equilibrium in each manifold.

The un-pumped uniform laser loss coefficient imposes a back-ground field dependence E $\propto$ $E \exp{(-\alpha_{0L}z/2)}$, where E is the slowly varying envelope field calculated in the FD-BPM (neglecting a rapidly varying phase term with imaginary exponent). The passive Cr^{4+}:YAG Q-switch similarly has an unsaturated absorption coefficient $\alpha_{0Q} = N_{Cr}\sigma_{gQ}$, and a field envelope relation E $\propto$ $E \exp{(-\alpha_{0Q}z/2)}$ in the FD-BPM. An energy level diagram for Cr^{4+} is shown by Burshtein *et al.* [35] and Xiao *et al.* [36]. In the rate-equation analysis, with very fast relaxation and thermalization among the highest levels, only two Cr^{4+} levels need be included - the ground state ($^3A_2$) and metastable state (^1E) with fractional population μ. Ridderbusch and Graf [37] show that only for picosecond pulses or extremely high intensity (not relevant to our model) are the highest excited Cr^{4+} population levels important. Further discussion of the Cr^{4+}:YAG energy levels may be found in refs. [7], [38]–[41]. There is variation in the literature concerning the Cr^{4+} saturable absorber ground- and excited-state absorption cross-sections; we have chosen to use the values cited in [3] and [4] to provide a basis for others who wish to compare results. Our data (Section IX) do not include laser polarization measurements, nor do we know the orientation of the Cr^{4+} saturable absorber crystal. The polarization-related references we cite may be of value for future use in modeling polarization-specific examples,

addressing the non-cubic symmetry of Cr^{4+} centers [38], [39], and in giving some measure of the uncertainty in our values. Such details are beyond the intended scope of this paper, but could be included in augmented rate equations within μ that include additional populated levels. However, if Cr^{4+} upper intra-manifold transition rates exceed the round-trip rate, then shorter computation time-step increments must be used, by means of multiple propagating-field-arrays discussed in Section X. The Cr^{4+} concentration, N_{Cr}, has not been included in Table I because we vary it to provide the desired Q-switch unsaturated transmission, for fixed Q-switch length.

Starting from an un-pumped state, we analyze the Yb^{3+} inversion increase as a pump absorption process, without any stimulated laser fields. The pump-only rate equations ignore amplified spontaneous emission, which is too weak to cause significant saturation effects. The pump is *not* modeled with BPM primarily because the pump field is not highly coherent. The pump spectrum is narrow-band (typically 0.2-0.3nm wide), and its fiber-combined high-power multiple diode emitter chips are not monochromatic. Also, we use diode sources coupled into a fiber with core diameter 105μm, whose output is then magnified and imaged into the Yb^{3+}:YAG crystal by an aspherical lens. The multi-mode nature of the fiber creates an incoherent, approximately circular spatial field with granular, speckle-like intensity output best treated with fine-scale transverse spatial averaging in a model for pump intensity. More experimental details are discussed in Section IX.

In our study we started with a simple approximation for the pump intensity, a constant-z profile with flat top near r = 0, and rounded edges. We used a Butterworth-like function to describe the pump beam, characterized by a specified full-width, half-maximum (FWHM) diameter and an adjustable rounding factor, the Butterworth function order. This is a rough depiction of geometric optics blurring of the fiber optic pump image in the few-mm-long crystal. The pump function remains normalized such that the integrated input power is constant, as either the FWHM or rounding is changed. The pump input function is

$$I_p(r) = \frac{P_{in}}{\pi r_0^2} \left[\frac{n \sin(2\pi/n)}{2\pi} \right] \frac{1}{1 + (r/r_0)^n},$$

with *n* ranging from 8 to 12, and input variable r_0 = FWHM/2. The bracketed expression is the power normalizing factor. As $n \to \infty$, the distribution approaches a flat-topped disk with steep edges. The same profile has been used as an example of high-power beam shaping within the different context of coherent beam propagation, where it was called a "super-Lorentzian" function [42]. Using any radial profile without longitudinal shape variation is particularly convenient for incorporating exact dynamic pump saturation with multiple (*r*-dependent) ordinary differential equations during the pre-lasing pump interval.

As an alternative to the above longitudinally uniform pump envelope shape, we have also used an approach to pump simulation which is more accurate in principal, but less convenient for parametric variation of the pump geometry. With a typical pump configuration (including the locations of fiber tip, aspheric transfer lens, pump-protection filter between the

fiber and the laser, and Yb:YAG crystal), a commercial ray-trace application [43] (including aspheric lens prescription) was used to simulate the un-attenuated pump power profiles at locations coincident with the FD-BPM longitudinal calculation planes and radial mesh points. The simulated fiber-coupled laser source is assumed to emit rays uniformly distributed over the multi-mode fiber core, with maximum ray angles corresponding to an NA ~ 0.10.

This method allows for more flexibility in using any desired longitudinal and radial variation of the pump distribution. Pump saturation effects are approximately included via space- and time-dependent population inversion factors which alter the local absorption in the rate equations (4) described below. Because of the short pump attenuation length, the front face of the laser crystal should be located approximately at the image waist of the pump fiber, with the desired magnification.

The Yb^{3+} rate equations use the gain and loss coefficients of the McCumber model for Yb^{3+}:YAG, and assume thermalized populations in the upper and lower Yb^{3+} manifolds, each characterized by a single population density variable. In the initial pump phase, the coherent laser fields are neglected, with only the Yb^{3+} inversion changing relatively slowly. A simpler set of rate equations is used to calculate the local pump intensity at all r, and integrates over time the r and z dependent normalized Yb^{3+} inversion

$$\rho = \frac{N\left(^2F_{5/2}\right)}{N\left(^2F_{5/2}\right) + N\left(^2F_{7/2}\right)} = \frac{N\left(^2F_{5/2}\right)}{N_{Yb}},$$

using coarse time steps about $0.25\mu s$ long. For *longitudinally varying pump shapes* the initial equations can incorporate a pump absorption dependent on $1 - \rho$, thus including pump saturation effects. Simple ray-gain estimates can be used to ensure that the pump-phase integration does not cause the laser threshold to be exceeded. Typically, the pre-lasing calculation interval may last several hundred microseconds. Since the Q-switching FD-BPM iterations are based on time increments of one round-trip (0.161ns in the following examples), much unnecessary coherent FD-BPM computation can be avoided using only the pump intensity (with no laser intensities in (4), and omitting the Q-switch terms).

After the end of the initial pump interval, pumping terms are still retained in the following population rate equations for any specified unsaturated input pump distribution; subsequent increase in ρ leads to gain build-up, Q-switch bleaching, Yb^{3+} gain depletion, and a similar repeating sequence of Q-switched pulses.

$$\frac{\partial \rho}{\partial t} = -\frac{I_{pump}}{h\nu_P}\left\{\sigma_{aP}\left(1 - \rho\right) - \sigma_{eP}\rho\right\}$$
$$-\frac{I_0 + I_1}{h\nu_L}\left\{\sigma_{eL}\rho - \sigma_{aL}\left(1 - \rho\right)\right\} - \frac{\rho}{\tau_{Yb}}$$
$$\frac{\partial \mu}{\partial t} = \frac{I_{Q0} + I_{Q1}}{h\nu_L}\sigma_{gQ}\left(1 - \mu\right) - \frac{\mu}{\tau_{Cr}}$$
$$g_{Yb} = N_{Yb}\rho\left(\sigma_{eL} + \sigma_{aL}\right)$$
$$g_Q = N_{Cr}\mu\left(\sigma_{gQ} - \sigma_{XQ}\right) \tag{4}$$

A key feature of our model is that all of the inversion factors and intensities in (4) are functions of r and z. Subscripts '0'

and '1' refer to intensities in the fundamental ($l = 0$) and 1st order ($l = 1$) angular momentum modes, having both radial (r) and longitudinal (z) dependence (in differenced form). Similarly, variables $\rho\left(r_i, z_j\right)$ and $\mu\left(r_i, z_j\right)$ occur at discrete times separated by the cavity round-trip time t_{RT}. Subscripts L, Q, and P refer to Laser, Q-switch, and Pump, respectively.

Equations (4) are updated by a simple Euler time-step increment t_{RT} after each round-trip propagation of the fields. All quantities depending on $\rho\left(r_i, z_j\right)$ and $\mu\left(r_i, z_j\right)$ are altered by the intensity-dependent terms, most importantly those affecting the complex refractive index difference and permittivity distribution ζ_m^q. The first right-hand-side term of (4) explicitly shows the saturation effects in the local pump absorption. The gain coefficients in (4) are the previously defined perturbation terms without uniform background loss. Each FD-BPM incremental propagation step makes the appropriate removal and restoration of the background loss to the total field from the envelope field.

During the transition from the first pump interval, and between Q-switched pulses, the populations change negligibly in t_{RT}, so the same coarse time increment can be used to update the populations in each BPM iteration. In the examples given here, the time increment in the build-up phase and between pulses is $2000 \times t_{RT}$. The coarse temporal step is necessary to complete the simulation within a practical time, since the interval between pulses is on the order of a few hundred μs. The transition between fine and coarse increments is automatically determined by a threshold-level crossing of the very small coherent field. Amplified spontaneous emission (dependent on ρ) is added to the $z = 0$ laser field when its amplitude is below a selected value, representing coupling from the total incoherent amplified spontaneous emission (ASE). During the long-increment intervals, the rate equations and FD-BPM steps start from the initial conditions of either the starting pump build-up or the previous Q-switch depleted inversion. The ASE-coupling addition dominates the initial condition in the field propagation equations for the long ($\sim 0.25 \mu s$) FD-BPM time steps. The fields are small, so saturation is negligible, and (4) is dominated by the pump and decay terms. As the gain increases towards the Q-switching threshold, the coherent fields begin to increase exponentially, and the calculations switch to use of t_{RT} time steps.

We believe it is important to apply the computation to as many sequential pulses as possible (subject to calculation time limitations), because the spatial and temporal Yb^{3+} inversion varies as the pulse train develops. The initial pulse is generated from an unsaturated gain state, but subsequent pulses will gradually accumulate both spatial and temporal saturation effects from previous pulses. At multi-kHz repetition rates, the $\sim 1ms$ radiative decay time of Yb^{3+} plays a significant role in determining the steady-state transverse spatial saturation profile. The constant temperature distribution (and thermal lensing contribution) is assumed to be the time-averaged temperature discussed below in Sec. V.

The boundary conditions in (3) can be set for either $l = 0$ or $l = 1$. If both modes are allowed to propagate simultaneously, then two separate BPM field solutions are calculated within each round-trip. The corresponding forward and backward

intensities are added for $l = 0$ and separately for $l = 1$ in the active media, and then combined in (4) to drive the population saturations. The $l = 1$ mode intensity from its BPM solution is multiplied by 2, to account for the $\pm l$ degeneracy of the solution. This is equivalent to adding $\sin^2 \phi$ and $\cos^2 \phi$ intensities, giving an azimuthally-independent saturation intensity, consistent with our radial symmetry assumption. The justification for adding the '0' and '1' *intensities* is that each radial BPM solution will have a different phase shift, in essence leading to differences in cavity quasi-resonant frequencies for different lateral modes. Intensity averaging neglects the effect of extremely high-frequency beating of the different modes. The approximate spatial orthogonality also minimizes the effects of inter-mode interference. In our cases of interest, when the $l = 0$ mode reaches threshold, bleaches the saturable absorber, and extracts inversion energy from the Yb^{3+} inversion, the subsequent gain is lowered sufficiently that the $l = 1$ mode does not reach threshold.

IV. RAPID THERMALIZATION

For the relatively short, high-loss cavities we are using, typical pulse widths are approximately 1.0-1.5 ns (FWHM). This raises the question whether the assumption of instantaneous (or very rapid) thermalization implicit in the McCumber theory is valid at such short times. Although there is no direct or obvious evidence to suggest otherwise, we wished to examine whether thermalization lag might impact the Q-switched behavior, particularly the pulse width. For example, as will be discussed in more detail later, the simulated temporal behavior of the pulse intensity shows an exponential build-up prior to the Q-switch transition (with rate mostly determined by the pumping parameters) and a more rapid post-pulse exponential decay (determined by the cavity output coupling and loss). There is no explicit published mention of which we are aware for such measured time asymmetry, although the behavior appears only in the pulse tails and may be obscured by the higher noise found in very-high-speed measurements.

Dynamic thermalization models have been developed in a plane-wave formalism for the lasing manifolds in Q-switched Nd^{3+} lasers by Degnan *et al.* [44] and Raikkonen *et al.* [45], whose methods we greatly simplified and adapted for Yb^{3+}. Both of those works derived an increase in pulse width if the thermalization rate was comparable to the inverse photon lifetime. We have done a similar analysis for Yb^{3+}:YAG with an approximate model having a few discrete levels in the upper and lower energy manifolds. Corresponding additional population variables were added to (4), with a rapid intra-manifold thermalization rate among them. Depending on the thermalization rate, small changes to the exponential pulse tails were found, but with more obvious changes to the pulse energy and repetition rate.

We may infer a bound on the thermalization effects from a logarithmic plot of pulse profile data shown in Fig. 4(b) of [2] (similar in qualitative behavior to results of our model calculation in Fig. 6 below). The exponential portion of the pulse decay was consistent with the high-cavity loss-rate, given the uncertainty in Q-switch excited-state absorption (ESA)
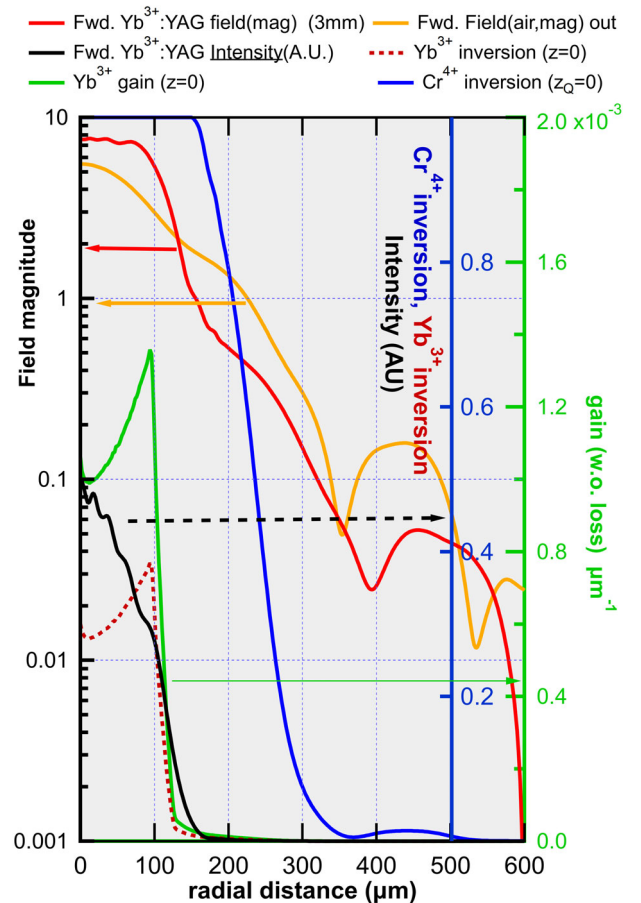

Fig. 4. Snap-shot radial profiles of field magnitudes and media variables at Q-switch peak with 26W pump. The radial scale has been expanded for clarity.

and other small parasitic cavity losses. We conclude that the measured fast trailing pulse decay is not slowed significantly by non-equilibrium inversion and gain replenishment from thermalization effects. Since there is no apparent thermalization broadening effect for the short 237ps pulses of [2], we expect even less consequence for the 1.0-1.5ns pulses of our longer lasers, and apply the usual McCumber thermal equilibrium model for absorption and emission cross-sections, shown in Fig. 3.

V. AVERAGE THERMAL EFFECTS ("THERMAL LENSING")

The complex permittivity allows for small changes from the real part of the refractive index. In our model these changes can occur from the local temperature dependence of an effective index of refraction, driven by heat deposition from the quantum defect of the pump beam. The pump beam is CW, and we neglect saturation and small temporal changes from variations in the Yb^{3+} ground-state population.

The main goal of our numerical model is to characterize the self-pulsing Q-switched laser in its fully evolved repetition state. To avoid the difficulties of calculating the time-dependent temperature from the initiation of the CW pump we assume a steady-state temperature distribution present at the start of the FD-BPM calculation, and driven by the quantum defect energy between the pump and laser

photons. This gives rise to a steady state heat deposition rate that is a fixed fraction of the *local* pump intensity. This simplification means that our calculated threshold build-up time, initial pulse intervals, and other early pulse properties are not expected to be as accurate as the longer duration results.

Thermal diffusion spreads the temperature profile and effectively smooths the high-spatial-frequency features present in the pump profile. One can approximate the thermal driving term by two different approaches. First is a top-hat radial heat distribution, with unsaturated exponential decay along the longitudinal (z) axis. In solving the cylindrically symmetric heat equation, we also neglect the longitudinal terms in the Laplacian operator. This is appropriate for the particular geometry we use: a small-diameter radial beam, with short transverse distance (1mm) to a $T = 273$K heat-sink, plus a long, slowly varying z-dependence in the pump absorption. The *normalized* transverse temperature solution profile is

$$T_{norm}(r) = \frac{1}{2}\left(1 - \frac{r^2}{r_0^2}\right) - \ln\left(\frac{r_0}{r_1}\right) \quad r \le r_0$$
$$= -\ln\left(\frac{r}{r_1}\right) \quad r > r_0 \qquad (5)$$

This use of only transverse heat spreading is also employed and justified in [18]. This method is simple and best suited for use with the Butterworth pump distribution.

The dimensionless profile is then multiplied by the product of (1): the initial pump quantum-defect power density, (2): $(dn/dT)_{eff}$, and (3): $\frac{r_0^2}{2\kappa}\exp(-\alpha_{0P}z)$ to give the spatial thermal refractive index perturbation $n_{re}(r, z)$. The effective thermal coefficient can include various components, such as thermal expansion and the stress-optic effect [13]–[15]; it is not necessarily the same as published *dn/dT*, and $(dn/dT)_{eff}$ is sometimes denoted as the thermo-optic coefficient, χ. The value we use from [16] is 1×10^{-5} K^{-1}.

The second approach for estimating the thermal distribution is more general, and uses the numerical pump beam profile calculated by the ray-trace method discussed above. In this instance, we *numerically* solve the transverse thermal diffusion equation

$$\frac{1}{r}\frac{\partial}{\partial r}\left(r\frac{\partial T}{\partial r}\right) \approx -\frac{q_{th}(r, z)}{\kappa}, \qquad (6)$$

and use the z-attenuated pump beam as the driving term for the thermal deposition $q_{th}(r, z)$ at each computational slice in the Yb^{3+}:YAG crystal. The RHS term is the quantum-defect fraction of the locally absorbed pump power per unit volume, divided by the thermal conductivity κ. The numerical solution (with outer heat-sink temperature as a boundary condition) uses a finite-difference tri-diagonal matrix method (similar to that for propagating the field), and allows for single pre-calculation of the real part of the spatially varying, time-averaged refractive index.

The steady-state thermal solution requires no time-step iteration. It uses a uniform constant heat sink temperature at the radial boundary. For either diffusion calculation method, we emphasize that neither a lumped, effective thermal focal length nor an effective radial phase-shift are calculated, as is common practice. Our distributed complex permittivity then includes the effects of real-valued *spatially distributed* thermal lensing from the thermal diffusion equation, as well as an imaginary permittivity component from the rate-equation gain/loss terms.

We have not included thermal effects on the absorption and emission cross-sections. Doing so would require more extensive data, particularly for the temperature dependent absorption spectra needed to derive the emission cross-sections. It should be possible to perform a one-time conversion of the present cross-section fixed parameters into spatially dependent functions, assuming the same time-averaged heat distribution used in the refractive index modeling.

VI. DIFFUSION OF EXCITATION

A potentially significant process (whose impact in Yb^{3+}:YAG lasers has yet to be measured) is the diffusion of localized regions of Yb^{3+} excitation. This process can occur by Forster resonance energy transfer (RET) from an excited site to an unexcited site by an electric dipole-dipole interaction [47]. With regions of spatially varying excitation comprising large number of ions the overall behavior is often characterized by a diffusion process. For our purposes, the critical aspects of this process are the spatial gradients and time scales over which the diffusion operates. In rare-earth-doped solid-state lasers this behavior has been analyzed with respect to spatial hole-burning of longitudinal gain by CW standing-wave cavity modes in Nd^{3+}:YAG lasers [48], [49]. The diffusion coefficient for those cases was quite small, $D \simeq 5.0 \times 10^{-7}$cm^2/s. Even though the distance between axial gain peaks was small (large spatial second derivatives), and the lasers were continuously on, this led to minimal diffusion, causing multi-longitudinal-mode oscillation not far above threshold. The main factor creating a small RET rate in Nd^{3+} is the small spectral overlap between the emission and absorption processes, since the terminal (absorptive) manifold in this 4-level system is minimally populated.

The situation with Yb^{3+} lasers is rather different. First, the spectral overlap between the emission and absorption cross-sections is orders of magnitude larger than Nd^{3+}, because absorption occurs from the ground-state manifold, containing the terminal levels for emission. Second, the Yb^{3+} concentration (10%) is larger than the typical 0.5% Nd^{3+} concentration, causing the most probable transfer distances to be much smaller. In work by Brenier [50], he finds the most probable migration rate to be

$$\frac{1}{\tau_o} = \frac{c\,N_{Yb}^2}{9\pi\,n^2}\int \sigma_e(\lambda)\,\sigma_a(\lambda)\,d\lambda.$$

To obtain the diffusion coefficient, D, dimensional analysis implies multiplying by the square of the most probable scaling distance between Yb^{3+} ions to get the correct dimensions of D (cm^2/s). A possible areal factor of 4π is already included in the migration rate. After performing the numerical spectral integration using our cross-section data, we calculate $D_{Yb} = 3.47 \times 10^{-3}$cm^2/s, almost four orders of magnitude larger than observed for Nd:YAG.

Diffusion may affect two aspects of our Q-switched lasers. The first effect is smoothing the transverse inversion depletion profile caused by saturation from the small-diameter laser-mode stimulated emission. The transverse depletion dimensions are 10's of μm wide, and the Q-switch pulse is about 1ns long so there is little diffusive impact during the pulse. In the much longer ($\sim$200μs) inter-pulse gain recovery, diffusion is a negligible process compared to the pump absorption replenishment of the inversion. In some of our simulations there were sharp transverse features in the saturated inversion (see Fig. (4) as an example). In the interval between pulses such features might be smoothed by diffusion, but we neglect such effects. The second effect is on the same longitudinal spatial hole-burning discussed above for Nd lasers. In this instance, the relevant time interval is the 1ns width of the Q-switch pulse. We calculate a small amount of hole-smoothing from diffusion; however, the net spatially integrated hole-burning is weakened by the strong longitudinal decay from pump absorption, and the weaker standing wave intensity amplitude in our low-reflectance, high-loss cavity. However, near the high-reflector laser mirror it may be possible for highly-saturated gain-competition to develop between such transient axial modes. We do expect the higher diffusion to lessen the longitudinal hole-burning for *low-loss*, *CW* Yb^{3+}:YAG lasers, increasing the tendency for single-longitudinal-mode operation in that regime.

VII. ANALYSIS OF COMPUTATION RESULTS

Accumulation of results over several sequential Q-switched pulses requires a large number of round-trip iterations, typically several thousand. It is not practical to store a full (r, z) complex data set for every iteration, so we process and extract only selected data that can be related to experimental measurements. Most of these data come from the transmitted intensity at the output mirror. For example, at each iteration the forward transmitted intensity from the last computation slice preceding the mirror is saved, to allow a 2D display of intensity *vs* radial coordinate and iteration index (kk). For convenience, the intensity is most conveniently displayed vs a fictitious uniform time scale with increment t_{RT} to show all the data and not compress the Q-switch pulses. Because the time increment multiplier varies in value, we also save an auxiliary array of absolute time *vs* kk for accurate determination of the pulse width and periodicity.

For the last Q-switched pulse, the output intensity for each mode is integrated (with radial weighting) over the 2D radial plane and multiplied by the round-trip time at each kk. Then the values of the radial integrations (energy/iteration) are summed over the times (iterations) between ASE threshold levels near the pulse base-line to obtain the pulse energy. To obtain the most typical results, the last pulse is selected because it is closest to a steady-state equilibrium limit determined by the effects of the Yb^{3+} relaxation time.

To evaluate the output pulse radial width, the radial-dependent intensities are first summed over time to obtain a time-integrated radial function. Then the full-width, half-maximum (FWHM) of that function is calculated. Similarly, we use the time-dependent energy/iteration output to find the temporal FWHM.

VIII. MODEL DEMONSTRATION EXAMPLE

Before describing the details of the laser construction and performance measurement (in Section IX below) we present simulation results for laser parameters that match the configuration for the measured data. A table of the variable input values (not provided in the previous Table) is shown below:

The pump distribution was presented in Fig. (2), derived from a ray-trace analysis of the imaged fiber pump source into the Yb^{3+}:YAG crystal. The effective FWHM pump diameter at $z = 0$ is 202μm.

The most detailed physical insight into the simulated laser operation is provided by a simultaneous monitoring of various radial functions as the Q-switch pulse is generated. A single-iteration snap-shot of that process at the maximum laser intensity is shown in Fig. 4 for the tenth pulse after the pump starts. Note that the field *magnitudes* are shown on a logarithmic scale (left axis) and the inversion and gain variables are shown on linear right axes. The longitudinal locations of the transverse profiles are displayed in the legend above the graph. Dynamic changes to this graph may be optionally viewed for selected FD-BPM iterations as the propagation code executes, but at the cost of graph update time. If graph updates are shown only during the Q-switch intervals this cost is relatively small.

The significant features in Fig. 4 are: (1) the Q-switch is fully saturated, with inversion fraction of 1; (2) the laser field has reached its maximum, with slight differences between the last field at the output of the Yb^{3+}:YAG, and the diffracted field at the 30% reflective mirror; and (3) the Yb^{3+} inversion has a non-uniformly saturated profile, with proportional reduction in the laser gain coefficient distribution. This non-uniform saturation has a significant effect in reducing the pulse energy which would be expected from a uniform plane-wave model. A *linear-scale forward intensity* curve (black, sharing the right-side blue axis) at $z = 3$mm in the Yb^{3+}:YAG crystal shows the relation to the adjacent saturation/gain curves. The CW pump replenishes the Yb^{3+} inversion between pulses, but a central depression remains. The Yb^{3+}:YAG dynamics are complicated by the fact that the Yb^{3+} radiative decay time ($\sim$1ms) is only a few times longer than a typical pulse period.

The sharp dips in the outer field magnitude curves qualitatively resemble sign-change locations of high-order radial mode admixtures to be expected in a modal expansion formalism. In the FD-BPM such sign changes are an intrinsic part of the self-consistent numerical field calculation. Different l-value solutions will have different radial distributions.

We have also compared the output energy of the optical pulse with the differential energy of the inversion before and after the Q-switch pulse. The difference in inversion density (ρ) is integrated over volume, and multiplied by the laser photon energy. For pump power between 14 and 26W, this optical-to-inversion ratio is nearly constant, from 0.873 to 0.892, consistent with a small amount of excess cavity diffraction, round-trip coupling, and absorption loss (particularly Q-switch ESA). The calculated fully saturated
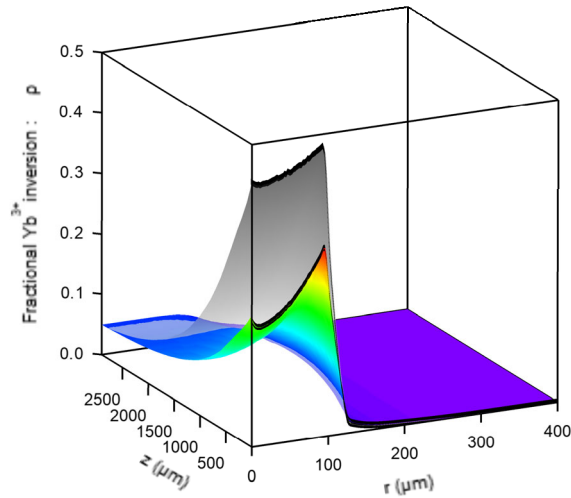
Fig. 5. Yb^{3+} inversion distributions (ρ) before and after Q-switch pulse: ρ(pre-pulse, gray scale), ρ(post-pulse, RGB scale); (expanded radial scale; black $z = 0$ surface edge boundaries). Pump power is 26W.

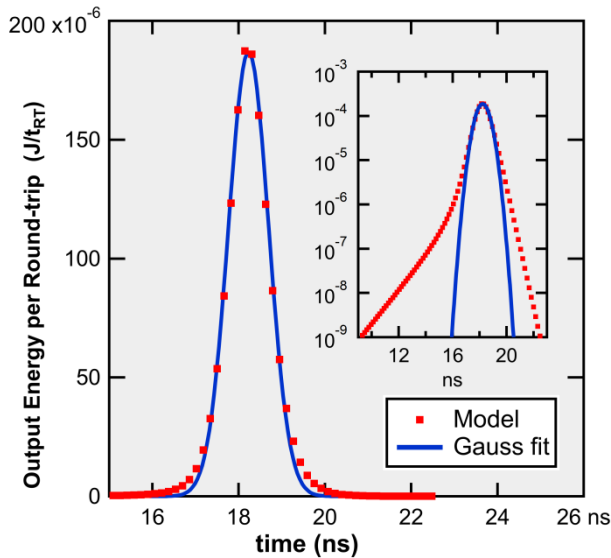Fig. 7. Near-field and far-field intensity profiles.

Fig. 6. Calculated time dependence of last output pulse. Inset: Intensity, with vertical logarithmic scale, to emphasize exponential-type edges.

round-trip Q-switch ESA loss is 0.068. An example of the two inversions is shown in Fig. 5 for 26W pump power.

Another measurable feature predicted by the model is the temporal profile of the output pulse. Contrary to many predictions and assumptions, the pulse does not have a Gaussian shape, although it may superficially appear so. This is shown in Fig. 6, where we plot the spatially integrated power density of the 12th pulse using 26W pump power, simulating full collection by a single high-speed detector (the arbitrary $t = 0$ origin has been shifted). Since the model operates with discrete high-resolution single-round-trip time steps during the pulses, we show the result as collected energy per round-trip interval, corresponding to samples of continuous power (W).

For comparison purposes, a Gaussian pulse with the same peak location, width and intensity is also shown. The latter is not a least-squares fit, but does have the best approximating width and position. A difference in the tail behavior is evident
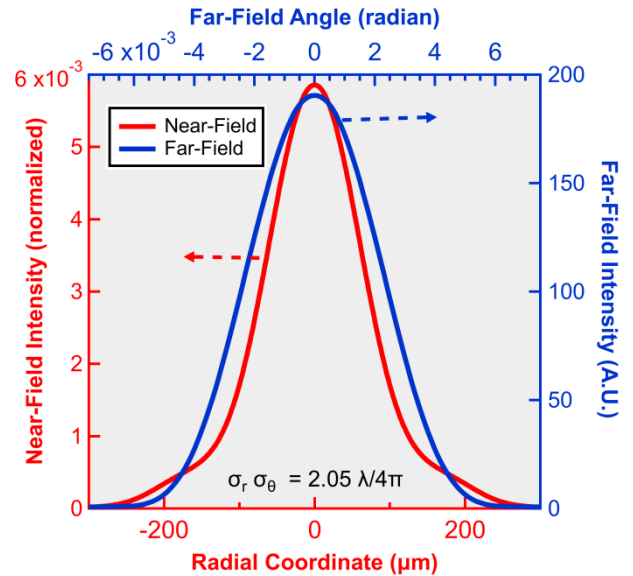
at the lower intensities. An inset plot with logarithmic intensity axis clearly shows exponential linear tails in the predicted model, consistent with a leading edge exponential build-up with a net gain coefficient, and a different decay rate during the post-pulse cavity loss per round trip (while the Q-switch remains saturated). The linear-axis large graph emphasizes the requirements in achieving sufficient measurement dynamic range and signal-to-noise to quantify the non-Gaussian characteristics.

Other predictions of the model (at the same 26W pump level) are the output near-field and far-field intensities, and the diffraction-limit relation between them. The near-field output intensity in Fig. 7 is the magnitude-squared of the output field shown in Fig. 4.

The complex output field itself also has a varying radial phase (including that of the output coupler's thin lens from its plano-convex shape). The complex far-field is calculated using the Fourier-Bessel transform of the complex near-field, which then provides the far-field intensity. The diffraction-limited performance is calculated using a version of the Weyl-Heisenberg Uncertainty Principle for the near-field spatial coordinate and conjugate far-field spatial angle [51]. From the Fourier-Bessel Transform properties and the Cauchy-Schwarz Inequality, the diffraction performance is provided by the numerically integrated variances (in two-dimensional r, θ space) of the radial and angular variables. Using the standard deviations for the usual form of the relation, the results shown in Fig. 7 have

$$\sigma_r \cdot \sigma_\theta = 2.05 \frac{\lambda}{4\pi},$$

which exceeds the minimum limit (for self-similar Gaussian near- and far-fields) with numerical coefficient 1.00. If the conventional use of $(1/e^2)$ limits had been used for both near- and far-fields, the diffraction-product coefficient would have been 1.70, a significant difference from the generalized variance analysis. The degradation from diffraction-limited
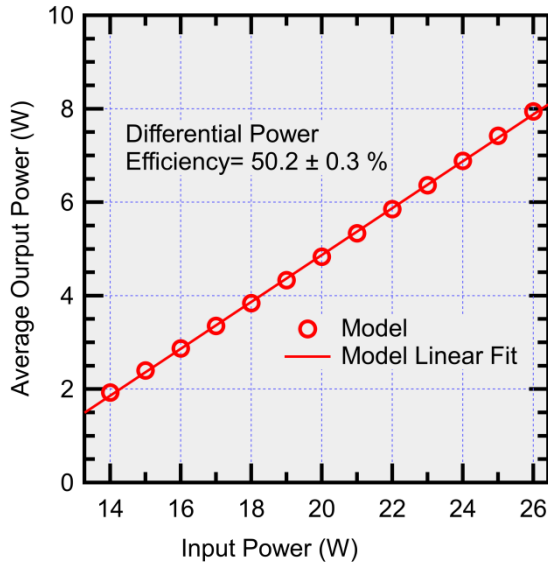
Fig. 8.   Calculated average laser output power vs CW pump power.

Fig. 9.   Pulse width, energy, and repetition rate vs pump power.

TABLE II

DEMONSTRATION EXAMPLE LASER PARAMETERS.

T_Q	Unsaturated, single-pass Q-switch intensity transmission		0.765
R_m	Output mirror reflectivity		0.3
R_{curv}	Output mirror convex radius of curvature	m	0.1
L_{Yb}	Yb^{3+}:YAG crystal length	mm	3.0
L_Q	Cr^{4+}:YAG crystal length	mm	2.0
L_{air}	Cavity air gap length	mm	15.0
P_{in}	Pump power input (940nm)	W	26.0

performance results from the combined effects of intensity and phase fluctuations across the complex near-field. In a very qualitative and approximate sense, these fluctuations may be thought of as an admixture of higher-order radial basis modes (all with $l = 0$, and at a common frequency), which are automatically incorporated by the numerical FD-BPM procedure. Note that in Fig. 4 the near-field magnitude profile at the output coupler differs from that in the Yb^{3+}:YAG crystal. The width and shape of the near-field depend heavily on the size of pump distribution and cavity parameters. The present example's laser parameters are chosen to match the experimental case discussed later. In many other instances with different cavity parameters and lower pump power, the calculated diffraction product is much closer to 1.

We have also examined several laser output variables as a function of pump power, particularly the average output power (shown in Fig. 8). The measured data for Figures 8 and 9 will be presented in Section IX below.

Other measureable variables *vs* pump power are shown in Fig. 9. The large increase in repetition rate reflects the faster Q-switch population recovery at increasing pump power. The increase of pulse energy with pump power may reflect changes due to thermal effects altering the mode shape and resulting energy extraction. The 0.1mm convex radius of the output coupler (held constant for this simulation) is meant to improve the laser performance at the maximum pump level by compensating for the largest anticipated thermal lensing; lower pump powers will decrease the thermal lensing effects, and may reduce the mode energy extraction. Simpler laser models (*e.g.* [8]) generally predict shorter pulse widths with higher energy extraction, which would be consistent with the trend in Fig. 9.

IX. EXPERIMENT DETAILS AND DATA

Development of the present modeling method was motivated by understanding experimental results from the Yb:YAG micro-laser described in the recently published Ref. [52].
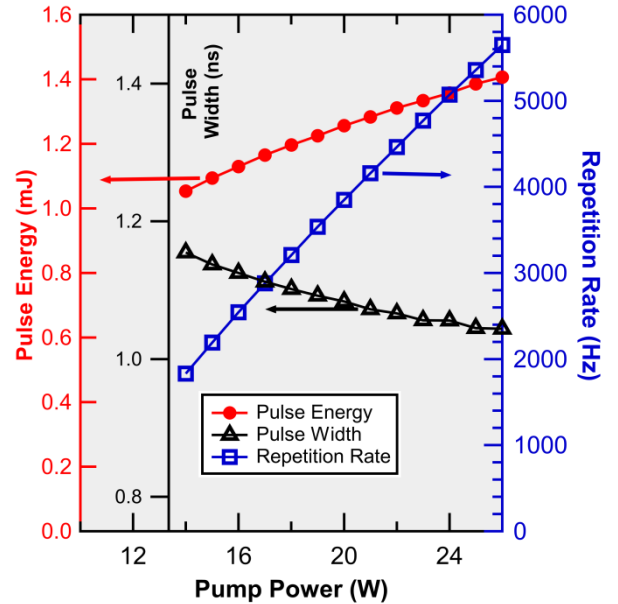
A CAD model of that laser configuration is shown in that reference's first figure. The fixed parameters in Table II were taken from [52]; comparison of model and data is primarily done with variable input power. Ref. [52] gives a $(1/e^2)$ pump diameter of 265μm, although we observe that this level is of limited value for quasi-top-hat pump power distributions of magnified fiber cores. A more useful pump measure is the input Full-Width, Half-Maximum (FWHM) which is smaller and closer to 200μm at a magnification near 2, with un-attenuated distribution shown in Fig. 2. The ray trace pump distribution used in the results below has an input FWHM diameter of 202μm, and a $(1/e^2)$ diameter of 229μm.

One of the significant results of our model is the sensitivity of some output parameters to the details of the pump distribution within the laser crystal. If the cavity is not the dominant factor in determining the laser mode profile, then the pump distribution becomes the most important factor. For a given pump power, the average output power of the laser may not vary significantly with small changes in effective pump diameter (the most significant impact is on laser threshold). However, the constituent pulse energy and repetition rate factors vary inversely to each other in a more significant way. A related issue affecting the model accuracy is the
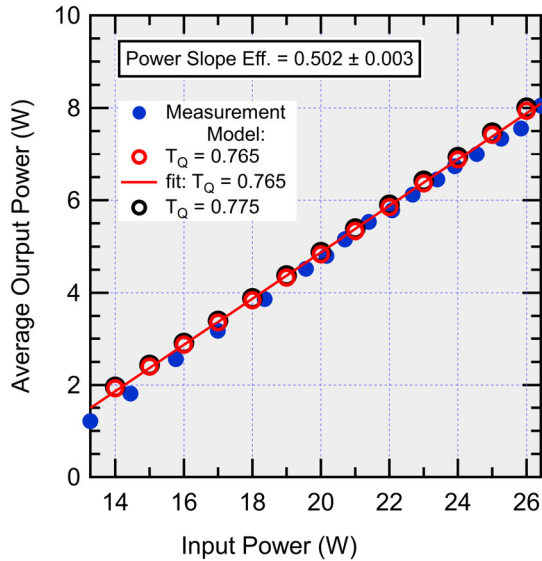
Fig. 10.   Average output power vs pump input power.

Fig. 11.   Optical power efficiency (output power/pump power) vs pump input power.

difficulty in setting or measuring the pump distribution, since it is extremely sensitive to sub-millimeter axial adjustments of the pump fiber tip and relay lens (which are difficult to measure). Typically, in the laboratory setting, laser operation is optimized by fine positioning the components in order to maximize the output power. From analyzing many ray-trace pump distributions, we believe that most efficient operation will be obtained with a relayed image of the pump fiber tip at the Yb:YAG high-reflector face (z = 0 in Fig. 1). Most of the pump power is absorbed in the first few hundred micrometers, so the shape of the uniform input beam and its quasi-collimation over most of the power absorption distance should lead to best performance.

Apart from the imaging details, there were no other adjustable parameters in the model. Another factor to keep in mind is that the measured data were also taken with fixed cavity and pump geometry parameters which were optimum for multi-Watt high power operation. At lower pump power levels optimized cavity parameters would be different.

The model results and measured data for average power output are shown in Fig. 10. This, and figure 12 below, also include results for a sensitivity analysis with $T_Q = 0.775$.

The efficiencies at each point in Fig. 10 are shown in Fig. 11.

A comparison of the model results from Fig.9 and data are shown in the following three figures.

Given that we have no adjustable parameters in the model (apart from the pump profile), these results show good agreement between model and data. The largest model discrepancies are (1) a consistently shorter pulse width (about 0.2-0.3 ns shorter calculated result), (2) a larger monotonic increase in pulse energy, and (3) a slightly lower pulse repetition rate with increasing pump power. These latter two results, however, produce an average power product in excellent agreement with the data. This may imply that the model's non-uniform spatial saturation of the gain profile is too large, since both the pulse energy and intra-pulse saturated recovery depend on
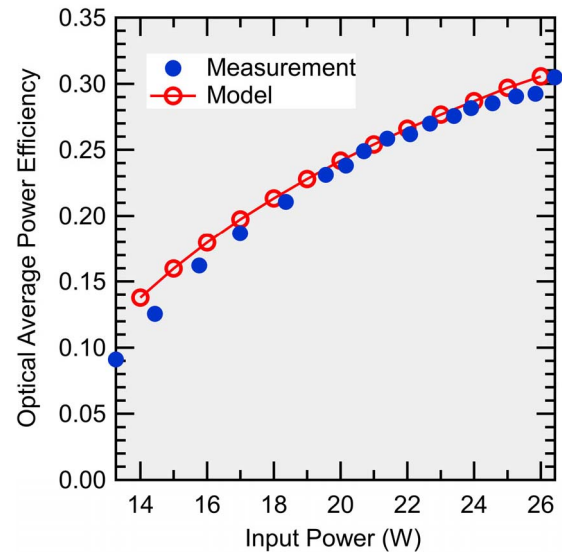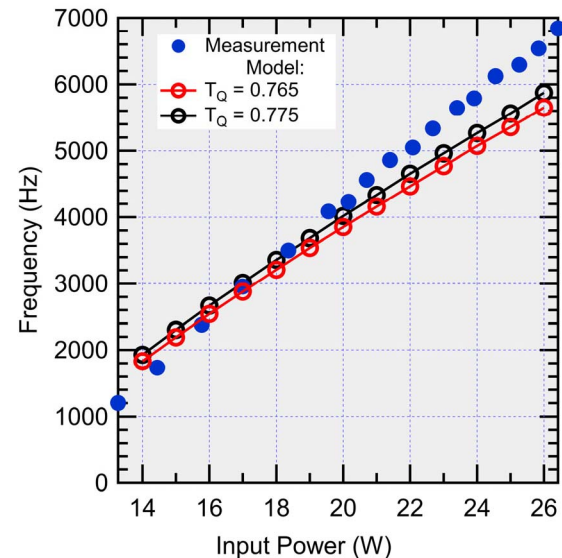

Fig. 12.   Frequency (pulse repetition rate) vs pump power.

this feature. Both model and data show a decreasing output mode diameter with increasing pump power, data showing a 25% decrease and model 4%. However, different mode-width criteria were used, and we believe the output mode to be non-Gaussian.

As an example of the importance of having accurate parameter values, we have checked the sensitivity to the unsaturated Q-switch transmission. Average power (Fig. 10) depends little on 1% increase of T_Q, but the repetition rate (Fig. 12) is noticeably sensitive to that change.

Another difference between data and model is in the diffraction product, whose modeled value was close to 2 throughout our pump power range. Results from [52] were $M^2 = 1.1$ at 5W output, degrading to 1.4 (vertical) at 10W. Ref. [52] used a different method of measuring the parameter through knife-edge scanning of projected near-field (NF) and far-field (FF) waists, whereas we use a rigorously correct method to
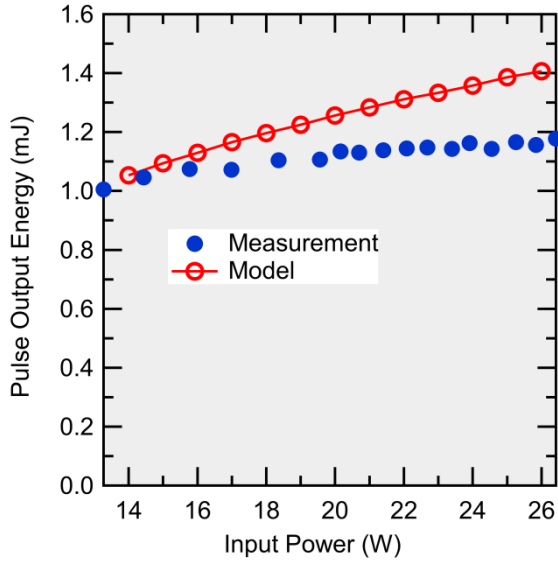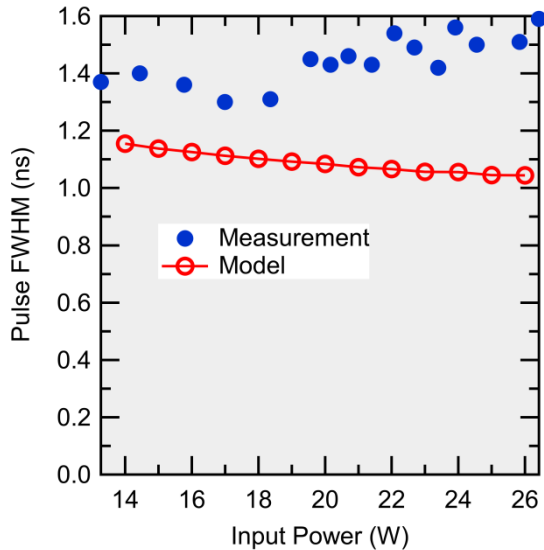
Fig. 13.   Pulse output energy vs pump power.

Fig. 14.   Pulse temporal FWHM vs pump power.

find normalized intensity 2nd moments (variances) through 2D NF and FF image intensity analysis. It should be noted that extracting accurate beam-shapes from knife-edge scans is difficult [53], [54], particularly with noisy or non-standard beams. Our model NF and FF profiles of Fig. 7 do not appear terribly degraded, but the NF intensity is clearly not Gaussian. We have previously commented on the potential inaccuracy of using $(1/e^2)$ waists for diffraction products from non-Gaussian beams. It should also be noted that the pump power for Fig.7 was 26W, close to an experimentally observed mode instability beyond that pump level. The model shows no evidence of such instability near 26W pump.

X. CONCLUSION

The most significant feature of our FD-BPM analysis described above is the quantitative inclusion of lateral and longitudinal non-uniformities in all relevant variables. In particular, this provides new insight into the saturation of the Yb^{3+} inversion by the laser field, and the subsequent effect of reduced laser energy extraction. The evolution of the laser mode(s) and gain extraction are intrinsically related by the coupled equations, and no separate gain-overlap integrals are required. As a result of the field/inversion coupling, we also find that the repetitive Q-switch output pulses themselves are not identical, but develop over a time-scale characteristic of the Yb^{3+} radiative lifetime. A steady-state pulse train does eventually result, but cannot be found using any *ab initio* assumptions, only from the multi-pulse numerical calculation. The coherent propagation method also allows for inclusion of intra-cavity diffraction effects, as well as quantitative far-field prediction.

Understanding the nature of the radial output field is important in predicting the energy extraction and the far-field beam quality. The size of the laser mode generally follows the size of the pump spot as long as output mirror curvature is small. Large pump diameters allow higher pulse energy, but with penalties of higher pump threshold power, lower repetition rate and degraded beam quality. The high loss associated with un-pumped regions in three-level lasers is favorable for suppressing high-order spatial modes, but the advantage decreases as the pump-region becomes too wide to maintain diffraction-limited mode quality. Spatial filtering techniques could be applied, but would reduce the amount of energy extraction.

We have chosen to use a minimum time increment of one round-trip; this requires only a single complex one-dimensional propagating field array, minimizes calculation time, and provides adequate temporal resolution even in our high-loss, short-pulse example. However, using several subdivided fields can provide higher resolution at the cost of increased computation complexity and time.

Another useful feature of the procedures developed above is the modular nature of various parts of the computation, e.g. for pumping, air gaps, reflective surface curvatures, and thermal analysis.

In its present form, the model does not explicitly treat the spectral dynamics of the laser. The FD-BPM calculation requires a choice of laser wavelength, which we take as the wavelength of peak gain under medium levels of Yb^{3+} inversion, 1030nm. The use of a coarse longitudinal computation grid with spacing of over 100 wavelengths does not allow for direct inclusion of longitudinal hole-burning effects at the 1/2 -wavelength scale. Similarly, the short laser photon cavity lifetimes do not permit iterative calculation of cavity axial resonances, particularly when the optical phase characteristics of the Q-switched laser medium are not constant, even within a single pulse. Another factor that may affect mode competition and stability is the polarization anisotropy of the Cr4+:YAG nonlinear absorption [40], [41]. The model presently operates with scalar field variables, although it might be augmented in a fashion similar to the inclusion of two azimuthal modes, if quantitative parameters for two orthogonal saturation polarizations were provided.

REFERENCES

[1] T. Y. Fan, S. Klunk, and G. Henein, "Diode-pumped Q-switched Yb:YAG laser," *Opt. Lett.*, vol. 18, no. 6, pp. 423–425, 1993.

[2] J. Dong, K. Ueda, A. Shirakawa, H. Yagi, T. Yanagitani, and A. A. Kaminskii, "Composite Yb:YAG/Cr^{4+}:YAG ceramics picosecond microchip lasers," *Opt. Express*, vol. 15, no. 22, pp. 14516–14523, 2007.

[3] J. Ma, J. Dong, K.-I. Ueda, and A. A. Kaminskii, "Optimization of yb:YAG/Cr^{4+}:YAG composite ceramics passively Q-switched microchip lasers," *Appl. Phys. B*, vol. 105, no. 4, pp. 749–760, Dec. 2011.

[4] M. Tsunekane and T. Taira, "High peak power, passively Q-switched Yb:YAG/Cr:YAG micro-lasers," *IEEE J. Quantum Electron.*, vol. 49, no. 5, pp. 454–461, Mar. 2013.

[5] J. J. Degnan, "Optimization of passively Q-switched lasers," *IEEE J. Quantum Electron.*, vol. 31, no. 11, pp. 1890–1901, Nov. 1995.

[6] F. D. Patel and R. J. Beach, "New formalism for the analysis of passively Q-switched laser systems," *IEEE J. Quantum Electron.*, vol. 37, no. 5, pp. 707–715, May 2001.

[7] A. Okhrimchuk and V. Shestakov, "The time and spatial dynamics of the YAG:Nd^{3+}/YAG:Cr^{4+} microchip laser emission," *Proc. SPIE*, vol. 6610, pp. 661002-1–661002-10, Apr. 2007.

[8] C. D. Nabors, "Q-switched operation of quasi-three-level lasers," *IEEE J. Quantum Electron.*, vol. 30, no. 12, pp. 2896–2901, Dec. 1994.

[9] X. Zhang, S. Zhao, and Q. Wang, "Modeling of passively Q-switched lasers," *J. Opt. Soc. Amer. B, Opt. Phys.*, vol. 17, no. 7, pp. 1166–1175, 2000.

[10] D. Gloge, "Weakly guiding fibers," *Appl. Opt.*, vol. 10, no. 10, pp. 2252–2258, 1971.

[11] T. Y. Fan, "Aperture guiding in quasi-three-level lasers," *Opt. Lett.*, vol. 19, no. 8, pp. 554–556, 1994.

[12] J. Delaney and J. Butler, "The effect of device geometry on lateral mode content of stripe geometry lasers," *IEEE J. Quantum Electron.*, vol. QE-15, no. 8, pp. 750–755, Aug. 1979.

[13] M. E. Innocenzi, H. T. Yura, C. L. Fincher, and R. A. Fields, "Thermal modeling of continuous-wave end-pumped solid-state lasers," *Appl. Phys. Lett.*, vol. 58, no. 19, pp. 1831–1833, 1990.

[14] J. Frauchiger, P. Albers, and H. P. Weber, "Modeling of thermal lensing and higher order ring mode oscillation in end-pumped C-W Nd:YAG lasers," *IEEE J. Quantum Electron.*, vol. 28, no. 4, pp. 1046–1056, Apr. 1992.

[15] T. Y. Fan, "Heat generation in Nd:YAG and Yb:YAG," *IEEE J. Quantum Electron*, vol. 29, no. 6, pp. 1457–1459, Jun. 2003.

[16] S. Chenais, F. Balembois, F. Druon, G. Lucas-Leclin, and P. Georges, "Thermal lensing in diode-pumped ytterbium lasers—Part I: Theoretical analysis and wavefront measurements," *IEEE J. Quantum Electron.*, vol. 40, no. 9, pp. 1217–1234, Sep. 2004.

[17] S. Chenais, F. Balembois, F. Druon, G. Lucas-Leclin, and P. Georges, "Thermal lensing in diode-pumped ytterbium lasers—Part II: Evaluation of quantum efficiencies and thermo-optic coefficients," *IEEE J. Quantum Electron.*, vol. 40, no. 9, pp. 1235–1243, Sep. 2004.

[18] S. Chenais, F. Druon, S. Forget, F. Balembois, and P. Georges, "On thermal effects in solid state lasers: The case of ytterbium-doped materials," *Prog. Quantum Electron.*, vol. 30, no. 4, pp. 89–126, 2006.

[19] E. Anashkina and O. Antipov, "Electronic (population) lensing versus thermal lensing in Yb:YAG and Nd:YAG laser rods and disks," *J. Opt. Soc. Amer. B, Opt. Phys.*, vol. 27, no. 3, pp. 363–369, 2010.

[20] X. Guo, S. Tokita, and J. Kawanaka, "High beam quality and high peak power Yb:YAG/Cr:YAG microchip laser," *Opt. Express*, vol. 27, vol. 1, pp. 45–54, 2019.

[21] M. Wohlmuth, "Modeling and simulation of solid-state laser resonators using a dynamic multimode analysis (DMA)," Ph.D. dissertation, Dept. Eng., Universität Erlangen-Nürnberg, Germany, München, 2012.

[22] M. Wohlmuth, C. Pflaum, K. Altmann, M. Paster, and C. Hahn, "Dynamic multimode analysis of Q-switched solid state laser cavities," *Opt. Express*, vol. 17, no. 20, pp. 17303–17316, 2009.

[23] M. Wohlmuth and C. Pflaum, "Dynamic multimode analysis of high-power 3-level lasers," *Phys. Procedia*, vol. 5, pp. 291–298, 2010.

[24] A. G. Fox and T. Li, "Modes in a maser interferometer with curved and tilted mirrors," *Proc. IEEE*, vol. 51, no. 1, pp. 80–89, Jan. 1963.

[25] A. Fox and T. Li, "Computation of optical resonator modes by the method of resonance excitation," *IEEE J. Quantum Electron.*, vol. 4, no. 7, pp. 460–465, Jul. 1968.

[26] G. R. Hadley, A. Owyoung, P. Esherick, and J. P. Hohimer, "Numerical simulation and experimental studies of longitudinally excited miniature solid-state lasers," *Appl. Opt., 27*, vol. 5, pp. 819–827, 1988.

[27] *Igor Pro Version 8.04*, WaveMetrics, Portland, OR, USA. [Online]. Available: https://www.wavemetrics.com/products/igorpro

[28] S. R. Chinn and V. King, "Subnanosecond (er,Yb) Glass Q-switched microlasers: 3-D transient modeling and experiments," *IEEE J. Quantum Electron.*, vol. 42, no. 11, pp. 1128–1136, Nov. 2006.

[29] G. R. Hadley, "Wide-angle beam propagation using Padé approximant operators," *Opt. Lett., 17*, vol. 20, pp. 1426–1428, 1992.

[30] J. Yamauchi, Y. Akimoto, M. Nibe, and H. Nakano, "Wide-angle propagating beam analysis for circularly symmetric waveguides: Comparison between FD-BPM and FD-TDM," *IEEE Photon. Technol. Lett.*, vol. 8, no. 2, pp. 236–238, Feb. 1996.

[31] G. R. Hadley, "Transparent boundary condition for beam propagation," *Opt. Lett.*, vol. 16, no. 9, pp. 624–626, 1991.

[32] G. R. Hadley, "Transparent boundary condition for the beam propagation method," *IEEE J. Quantum Electron.*, vol. 28, no. 1, pp. 363–370, Jan. 1992.

[33] D. C. Brown, R. L. Cone, Y. Sun, and R. W. Equall, "Yb:YAG absorption at ambient and cryogenic temperatures," *IEEE J. Sel. Topics Quantum Electron.*, vol. 11, no. 3, pp. 604–612, May 2005.

[34] D. Kouznetsov, "Broadband laser materials and the McCumber relation," *Chin. Opt. Lett.*, vol. 5, no. 101, pp. S240–S242, 2007.

[35] Z. Burshtein, P. Blau, Y. Kalisky, Y. Shimony, and M. R. Kikta, "Excited-state absorption studies of Cr^{4+} ions in several garnet host crystals," *IEEE J. Quantum Electron.*, vol. 34, no. 2, pp. 292–299, 1998.

[36] G. Xiao, J. H. Lim, S. Yang, E. Van Stryland, M. Bass, and L. Weichman, "Z-scan measurement of the ground and excited state absorption cross sections of Cr^{4+} in yttrium aluminum garnet," *IEEE J. Quantum Electron.*, vol. 35, no. 7, pp. 1086–1091, Jul. 1999.

[37] H. Ridderbusch and T. Graf, "Saturation of 1047- and 1064-nm absorption in Cr^{4+}:YAG crystals," *IEEE J. Quantum Electron.*, vol. 43, no. 2, pp. 168–173, Feb. 2007.

[38] H. Eilers, U. Hömmerich, S. M. Jacobsen, and W. M. Yen, "Spectroscopy and dynamics of Cr^{4+}:$Y_3Al_5O_{12}$," *Phys. Rev. B, Condens. Matter*, vol. 49, no. 22, pp. 15505–15513, 1994.

[39] A. G. Okhrimchuk and A. V. Shestakov, "Absorption saturation mechanism for YAG:Cr^{4+} crystals," *Phys. Rev. B, Condens. Matter*, vol. 61, no. 2, pp. 988–995, 2000.

[40] H. Eilers, K. R. Hoffman, W. M. Dennis, S. M. Jacobsen, and W. M. Yen, "Saturation of 1.064 μm absorption in Cr,Ca:$Y_3Al_5O_{12}$ crystals," *Appl. Phys. Lett.*, vol. 61, no. 25, pp. 2958–2960, 1992.

[41] H. Sakai, A. Sone, H. Kan, and T. Taira, "Polarization stabilizing for diode-pumped passively Q-switched Nd:YAG microchip lasers," *Opt. Soc. Amer. Adv. Solid-State Photon.*, 2006, Paper MD2. [Online]. Available: https://www.osapublishing.org/abstract.cfm?uri=ASSP-2006-MD2

[42] D. L. Shealy and J. A. Hoffnagle, "Beam shaping profiles and propagation," *Proc. SPIE, Laser Beam Shaping VI*, Aug. 2005, Art. no. 58760D.

[43] *OpticStudio*, Zemax LLC., Kirkland, WA, USA. [Online]. Available: www.zemax.com

[44] J. J. Degnan, D. B. Coyle, and R. B. Kay, "Effects of thermalization on Q-switched laser properties," *IEEE J. Quantum Electron.*, vol. 34, no. 5, pp. 887–899, May 1998.

[45] E. Raikkonen, S. C. Buchter, and M. Kaivola, "Modeling the time-dynamics of miniature passively Q-switched lasers," *IEEE J. Quantum Electron.*, vol. 45, no. 12, pp. 1563–1570, Dec. 2009.

[46] D. C. Brown and V. A. Vitali, "Yb:YAG kinetics model including saturation and power conservation," *IEEE J. Quantum Electron.*, vol. 47, no. 1, pp. 3–12, Jan. 2011.

[47] D. L. Andrews, "Resonance energy transfer: Theoretical foundations and developing applications," in *Tutorials in Complex Photonic Media*, vol. PM194, M. A. Noginov, G. Dewar, M. W. McCall, and N. I. Zheludev, Eds. Bellingham, WA, USA: SPIE, 2009, ch. 14.

[48] H. G. Danielmeyer, "Effects of drift and diffusion of excited states on spatial hole burning and laser oscillation," *J. Appl. Phys.*, vol. 42, no. 8, pp. 3125–3132, Jul. 1971.

[49] J. J. Zayhowski, "The effects of spatial hole burning and energy diffusion on the single-mode operation of standing-wave lasers," *IEEE J. Quantum Electron.*, vol. 26, no. 12, pp. 2052–2057, 1990.

[50] A. Brenier, "Excited-state dynamics including radiative diffusion in quasi-three-level laser crystals: Application to Yb^{3+}-doped $Y_3Al_5O_{12}$," *J. Opt. Soc. Amer. B, Opt. Phys.*, vol. 23, no. 10, pp. 2209–2216, 2006.

[51] E. Candes. (2016). *Applied Fourier Analysis and Elements of Modern Signal Processing*. [Online]. Available: https://statweb.stanford.edu/~candes/math262/Lectures/Lecture04.pdf

[52] C. McIntosh, A. D. Hays, R. Stephen Chinn, L. Goldberg, and J. Leach, "High average power passively Q-switched Yb:YAG micro-laser," *Proc. SPIE*, vol. 11259, Feb. 2020, Art. no. 112590W.

[53] A. E. Siegman, M. W. Sasnett, and T. F. Johnston, "Choice of clip levels for beam width measurements using knife-edge techniques," *IEEE J. Quantum Electron.*, vol. 27, no. 4, pp. 1098–1104, Apr. 1991.

[54] R. M. O'Connell and R. A. Vogel, "Abel Inversion of knife-edge data from radially symmetric pulsed laser beams," *Appl. Opt.*, vol. 26, no. 13, pp. 2528–2532, 1987.

Stephen R. Chinn (Life Senior Member, IEEE) was born in Baltimore, MD. He received the B.S., M.S., and Ph.D. degrees in electrical engineering from the Massachusetts Institute of Technology (MIT), Cambridge, MA.

He has worked at AT&T Bell Laboratories, MIT Lincoln Laboratory, and the General Electric Electronics Laboratory. He has been with the US Army DEVCOM C5ISR Night Vision and Electronic Sensors Directorate since 2002, as a civilian employee and Contractor, where he performs research and development on advanced laser and electro-optic sensor systems.

Jeffrey H. Leach received the M.S. and Ph.D. degrees in electrical engineering from the Virginia Polytechnic Institute and State University, Blacksburg, VA, and the Catholic University of America, Washington, D.C., respectively.

He focused on electro-optics of lidar systems. He has been with the US Army DEVCOM C5ISR Night Vision and Electronics Sensors Directorate as an Electronics Engineer at Ft Belvoir, VA, since 2003. He currently works on robust electro-optic systems.

Chris McIntosh received the M.S. and Ph.D. degrees in physics from Lehigh University.

He worked on laser diode packaging and fiber lasers at Keopsys from 2001 to 2007. He has worked for the US Army DEVCOM C5ISR Night Vision and Electronic Sensors Directorate since 2007, where he performs research on solid-state lasers and LADAR systems.

A. D. Hays received the M.S. degree in physics from the University of South Florida, Tampa, in 1987, and the Ph.D. degree in electrical engineering from the Catholic University of America, Washington D.C., in 2015.

He studied opto-thermal stresses, and methods for improving laser brightness. In 2001, he joined the US Army DEVCOM C5ISR Night Vision and Electronics Sensors Directorate as a Research Scientist at Ft Belvoir, VA. He currently works on compact solid-state lasers and electro-optic systems.

Lew Goldberg was born in Chervyen, Belarus. He received the B.S. degree in electrical engineering from Tufts University in 1973, the M.S. degree in electrical engineering from Carnegie Mellon University in 1974, and the Ph.D. degree in applied physics from the University of California San Diego in 1979.

He has worked as an Assistant Professor with UCSD in 1980, at the Naval Research Laboratory from 1980 to 2000, at Keopsys Inc. from 2000 to 2005 and at the US Army DEVCOM C5ISR Night Vision and Electronic Sensors Directorate since 2005, where he is the Head of the Laser Branch, performing research and development on advanced laser and electro-optic devices and systems.